JOURNAL OF MATERIALS SCIENCE **36** (2001) 2851 – 2863

A crystal plasticity materials constitutive model for polysynthetically-twinned γ-TiAl + α_2-Ti_3Al single crystals

M. GRUJICIC, S. BATCHU
Department of Mechanical Engineering, Program in Materials Science and Engineering, Clemson University, Clemson, SC 29634, USA

Deformation behavior of polysynthetically-twinned lamellar γ-TiAl + α_2-Ti_3Al single crystals has been analyzed using a three-dimensional, isothermal, rate-dependent, large-strain, crystal-plasticity based materials constitutive model. Within the model it is assumed that plastic deformation parallel to the γ-TiAl/α_2-Ti_3Al lamellar boundaries is controlled by the softer γ-TiAl phase while deformation which contains a component normal to these boundaries is dominated by the harder α_2-Ti_3Al phase. The parameters appearing in the crystal-plasticity materials constitutive relations are assessed using the available experimental information pertaining to the active slip systems, their deformation resistances and hardening and rate behavior of the two constitutive phases both in their single-crystalline and in polysynthetically-twinned lamellar forms. The constitutive relations are implemented in a Vectorized User Material Subroutine (VUMAT) of the commercial finite element program Abaqus/Explicit within which the material state is integrated during loading using an explicit Euler-forward formulation. The results obtained suggest that the adopted crystal-plasticity model and the parameters assessed in the present work account quite well for the observed room-temperature deformation behavior of polysynthetically-twinned lamellar γ-TiAl + α_2-Ti_3Al single crystals.

1. Introduction

Two-phase γ-TiAl + α_2-Ti_3Al alloys with micron-scale lamellar microstructures generally exhibit improved ductility and fracture toughness in comparison to their monolithic constituents. In addition, these alloys possess a superior combination of high-temperature properties such as creep resistance, microstructural stability, oxidation resistance, etc. Consequently, there has been much interest in developing these alloys as viable materials for high-temperature structural applications. There are several comprehensive reviews [e.g. 1–3], that summarize major advances in development of these alloys. It should be pointed out, however, that the main improvements in alloy properties have been realized largely in polysynthetically twinned single-crystalline form of these materials and that it has been quite difficult to obtain similar successes in the polycrystalline materials of this type. The latter typically fail at tensile strains less than 3% and have a low level of fracture toughness with the critical stress intensity factor K_{IC} being generally less than 30 MPa $\sqrt{m}$. In addition, many properties (e.g. tensile fracture strain, fracture toughness, etc.) of γ-TiAl + α_2-Ti_3Al single crystals are highly anisotropic. While the single crystalline materials possess quite attractive properties, their use is cost prohibitive. Thus, achieving a superior combination of properties in conventionally processed polycrystalline γ-TiAl + α_2-Ti_3Al alloys remains an important, though formidable, engineering challenge. Nevertheless, better understanding of the physical basis for improved performance of polysynthetically-twinned γ-TiAl + α_2-Ti_3Al single crystals, and their high level of anisotropy, which is the subject of the present work, should certainly assist the development of high-performance polycrystalline alloys of this type.

During solidification, Ti-(48–50 at.%) Al alloys, which are considered in the present work, form a disordered hexagonal-close-packed (h.c.p.) α-phase which upon cooling orders into a h.c.p.-based α_2-phase with the DO_{19} crystal structure and then transforms to (or near) completion into an ordered face-centered-tetragonal (f.c.t.) γ-phase with the $L1_0$ crystal structure. The final microstructure consists of parallel γ-TiAl and α_2-Ti_3Al lamellae with a standard f.c.c.-h.c.p. type orientation relationship: $\{111\}\gamma \parallel (0001)\alpha_2$ and $\langle 1\text{–}10]\gamma \parallel \langle 11\text{–}20\rangle\alpha_2$. In addition, the α_2/γ and γ/γ lamellar interfaces acquire a $\{111\}\gamma \parallel (0001)\alpha_2$ and a $\{111\}\gamma \parallel \{111\}\gamma$ orientation, respectively [4]. This implies that the unique orientation of the basal (0001) plane in each grain of the parent h.c.p. α-phase dictates the orientation of the resulting γ-TiAl and α_2-Ti_3Al lamellae.

The mechanical response of single-crystalline γ-TiAl + α_2-Ti_3Al materials is highly anisotropic at the macroscopic, microscopic and crystal structure length scales. At the macroscopic length scale, properties such as flow stress, fracture stress, fracture strain, critical stress intensity factor, crack growth rate, and others exhibit a strong orientation dependence [e.g. 5]. In the γ-TiAl + α_2-Ti_3Al laminar microstructure, γ-TiAl is the softer phase and its flow properties are highly anisotropic due to the lamellar geometry. Shear deformation parallel to the lamellar interfaces is considerably easier (the soft mode) than that normal to the interfaces (the hard mode). In the latter case, slip in γ-TiAl encounters the harder α_2-Ti_3Al phase [6]. Since the soft-to-hard mode slip length ratio is typically on the order of 100, the Hall-Petch effect is significant [7]. In addition, the Hall-Petch slope is also anisotropic, with typical values 0.273 and 0.440 MPa/$\sqrt{}$m for the soft and the hard modes, respectively [7]. Thus, the microscopic length-scale anisotropy largely pertains to large differences in the soft- and hard-mode deformation resistances within each phase and to the differences in deformation resistances of the two phases. At the crystal structure length-scale, anisotropy arises from the differences in deformation resistance of different slip systems within the same phase. For example, $\langle a \rangle$-slip systems associated with $\langle 11\bar{2}0 \rangle$ slip directions are generally substantially softer than any of the possible $(c+a)$-slip systems in α_2-Ti_3Al. Since the latter systems are needed to achieve a general state of strain, during plastic deformation the α_2-Ti_3Al phase can be considered as kinematically constrained in the c-direction. The behavior of the materials is further complicated by the fact that the contribution of a particular slip system to the overall deformation is affected by temperature, strain rate, alloy chemistry and more importantly, the impurity content.

Micromechanics-based finite element analyses which use physically-based materials constitutive relations for the constituent phases, enable incorporation of the orientation relationships between the phases, orientation of the phase boundaries, and various kinematic constraints (e.g. α_2/γ interfaces must remain of the $(0001)_{\alpha 2} \parallel \{111\}_\gamma$ character) offer a unique opportunity to better understand the deformation and fracture behavior of polysynthetically–twinned single-crystalline γ-TiAl + α_2-Ti_3Al alloys. Such analyses were conducted in a series of papers by Asaro and coworkers [e.g. 8–10]. However, Asaro and coworkers analyzed primarily the effect of grain misorientation on the local incompatibility of plastic flow and on the resulting stress concentration which can lead to material fracture in polycrystalline γ-TiAl + α_2-Ti_3Al alloys. In addition, a two-dimensional idealization of the crystallographic-slip behavior in a homogenized γ-TiAl + α_2-Ti_3Al material was used by these investigators which prevents a more direct comparison of the computed results and their experimental counterparts. To overcome these limitations, a full three-dimensional analysis of the slip behavior in γ-TiAl and α_2-Ti_3Al single crystals is carried out within the framework of crystal plasticity. The results obtained are used to construct a homogenized crystal-plasticity based materials constitutive model for polysynthetically-twinned γ-TiAl + α_2-Ti_3Al single crystals. The kinematic coupling between the two phases is incorporated by requiring that slip parallel to the lamellar interfaces is dominated by the softer γ-TiAl phase, while slip normal to these interfaces is taken to be controlled by the harder α_2-Ti_3Al phase.

The organization of the paper is as follows: The basic deformation behaviors of γ-TiAl and α_2-Ti_3Al single crystals by crystallographic slip are described in Section 2.1. The deformation behavior of polysynthetically-twinned γ-TiAl + α_2-Ti_3Al single crystals by slip is discussed in Section 2.2. A brief overview of the crystal-plasticity materials constitutive relations for γ-TiAl and α_2-Ti_3Al single crystals as well as for polysynthetically-twinned γ-TiAl + α_2-Ti_3Al single crystals and their implementation into the commercial finite element package Abaqus/Explicit [11] are outlined in Section 2.3 and in Appendix A, respectively. The procedure for the assessment of the crystal-plasticity parameters and the main computational results and their comparison with the experimental counterparts are discussed in Section 3 and in Appendix B. The main conclusions resulting from the present work are presented in Section 4.

2. Computational procedure

2.1. Deformation behavior of γ-TiAl and α_2-Ti_3Al single crystals

The γ-TiAl phase has an ordered f.c.t.-based $L1_0$ crystal structure, Fig. 1a, with $c_\gamma/a_\gamma = 1.02$ and $a_\gamma = 0.4$ nm where a_γ and c_γ are the lattice parameters. In the single-crystalline form of γ-TiAl, the inelastic deformation of this phase is mainly the result of $b = 1/2\langle 1\bar{1}0 \rangle$ ordinary-dislocation slip (b—the magnitude of the Burgers vector) with an additional contribution from $b = \langle \bar{1}01 \rangle$ super-dislocation and a limited contribution from $b = 1/2\langle \bar{1}\bar{1}2 \rangle$ ordinary-dislocation slip, all on the {111} family of planes, Fig. 2, [6]. A mixed $\langle \cdots \rangle/[\cdots]$. notation as in $\langle 1\bar{1}0 \rangle$ is used to make distinction between the first two Miller indices and the third one. This is needed when identifying crystallographically equivalent directions in a tetragonal crystal structure such as that of γ-TiAl. It should be noted that twinning, though not considered in the present analysis, can play a role especially at lower temperatures and higher deformation rates.

The native basis of the f.c.t. crystal structure is orthogonal and is defined by base vectors $\{\mathbf{a}^\gamma, \mathbf{b}^\gamma, \mathbf{c}^\gamma\}$, Fig. 2. To obtain an orthonormal basis which is needed for computations, the following normalization must be done: $e_1^\gamma = \mathbf{a}^\gamma/a^\gamma$, $e_2^\gamma = \mathbf{b}^\gamma/a^\gamma$, $e_3^\gamma = \mathbf{c}^\gamma/c^\gamma$ where $\{e_1^\gamma, e_2^\gamma, e_3^\gamma\}$ are the unit base vectors of the orthonormal coordinate system.

The α_2-Ti_3Al phase possesses an ordered h.c.p.-based DO_{19} crystal structure, Fig. 1b, with $c_{\alpha 2}/a_{\alpha 2} = 0.8$ and $a_{\alpha 2} = 0.577$ nm, where $a_{\alpha 2}$ and $c_{\alpha 2}$ are the lattice parameters. The plastic deformation in this phase takes place largely on the prismatic $\{10\ \bar{1}\ 0\}\ \langle 1\ \bar{2}\ 10 \rangle$ and the basal $(0001)\ \langle 11\ \bar{2}\ 0 \rangle$ $\langle a \rangle$-slip systems and on

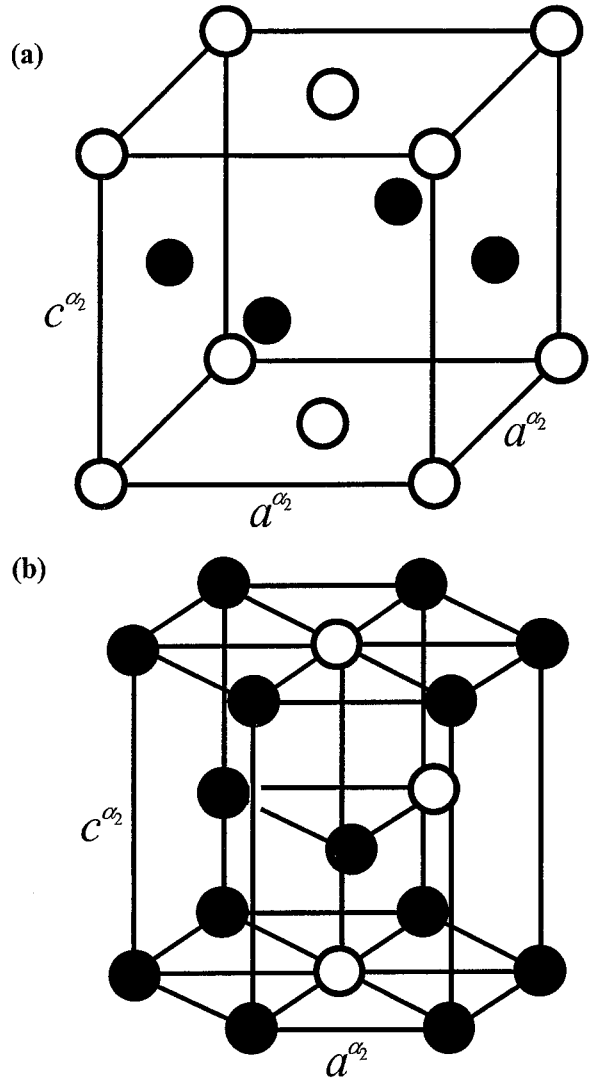

Figure 1 The crystal structures of the (a) $L1_0$ γ-TiAl and (b) DO_{19} α_2-Ti_3Al: Al atoms—open circles, Ti atoms—filled circles.

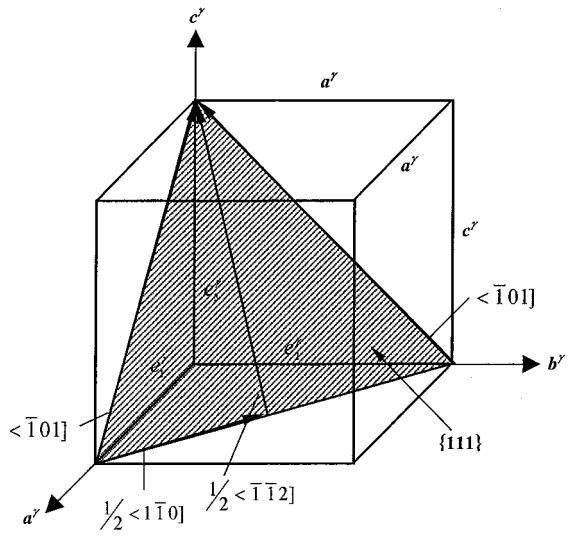

Figure 2 The relationship between the orthogonal $\{a^\gamma, b^\gamma, c^\gamma\}$ and the orthonormal $\{e_1^\gamma, e_2^\gamma, e_3^\gamma\}$ coordinate systems and the active slip systems in γ-TiAl.

the pyramidal $\{11\ \bar{2}\ 1\}\ \langle 11\ \bar{2}\ 6\rangle$ $\langle c+a\rangle$-slip system, Fig. 3a–c [9, 10]. The α_2-Ti_3Al phase in equilibrium with the γ-TiAl phase in polysynthetically-twinned γ-TiAl + α_2-Ti_3Al single crystals typically contains 36.5 at. % Al. For the α_2-phase of this composition, the ambient-temperature critical resolved shear stresses for the prismatic $\{10\ \bar{1}\ 0\}\ \langle 1\ \bar{2}\ 10\rangle$, the basal $(0001)\ \langle 11\,\bar{2}\,0\rangle$ and the pyramidal $\{11\ \bar{2}\ 1\}\ \langle 11\ \bar{2}\ 6\rangle$ slip systems, are found to be 100, 330, and 910 MPa, respectively [10]. As mentioned earlier, due to the unusually high value of the critical resolved shear stress for the $\{11\ \bar{2}\ 1\}\ \langle 11\ \bar{2}\ 6\rangle$ $(c+a)$-slip system, the plastic deformation is essentially constrained in the c-direction of the α_2-Ti_3Al phase.

The native lattice basis of the h.c.p. crystal structure is non-orthogonal. This basis is denoted in Fig. 3d by a set of non-orthogonal base vectors, $\{\mathbf{a}_1, \mathbf{a}_2, \mathbf{a}_3, \mathbf{c}\}$ with $\mathbf{a}_1 + \mathbf{a}_2 + \mathbf{a}_3 = 0$. For computational purposes, an orthonormal basis is generally needed. Toward that end an orthohexagonal cell is first defined. Fig. 3d shows the relationship between a simple hexagonal cell defined by the base vectors $\{\mathbf{a}_1, \mathbf{a}_2, \mathbf{a}_3, \mathbf{c}\}$ and the corresponding orthohexagonal cell defined by the base vectors $\{\mathbf{a}^{\alpha 2}, \mathbf{b}^{\alpha 2}, \mathbf{c}^{\alpha 2}\}$. The two cells share the base vector $\mathbf{c}$ while the other base vectors are related as: $\mathbf{a}^{\alpha 2} = \mathbf{a}_2$, and $\mathbf{b}^{\alpha 2} = \mathbf{a}_3 - \mathbf{a}_1$. The needed orthonormal cell is then defined by the unit base vectors $\{e_1^{\alpha 2}, e_2^{\alpha 2}, e_3^{\alpha 2}\}$ which are obtained by the following normalization: $e_1^{\alpha 2} = \mathbf{a}^{\alpha 2}/|\mathbf{a}^{\alpha 2}|$, $e_2^{\alpha 2} = \mathbf{b}^{\alpha 2}/|\mathbf{b}^{\alpha 2}|$, and $e_3^{\alpha 2} = \mathbf{c}/\mathbf{c}^{\alpha 2}$.

2.2. Deformation behavior of polysynthetically-twinned γ-TiAl + α_2-Ti_3Al single crystal

A schematic of the typical microstructure of polysynthetically-twinned γ-TiAl + α_2-Ti_3Al single crystals is shown in Fig. 4. The microstructure consists of a single set of parallel γ-TiAl and α_2-Ti_3Al lamellae. Typically, the number of γ-TiAl lamellae is an order of magnitude larger than the number of α_2-Ti_3Al lamellae. As pointed out earlier, the lamellae of the two phases have a $(111)_\gamma \parallel (0001)_{\alpha 2}$ and $\langle 1\text{–}10]_\gamma \parallel \langle 11\text{–}20\rangle_{\alpha 2}$ orientation relationship and the lamellae interfaces are parallel with the $(111)_\gamma \parallel (0001)_{\alpha 2}$ planes. It should be noted that close-packed $\langle 11\text{–}20\rangle_{\alpha 2}$ directions are all equivalent, while, due to tetragonality of the $L1_0$ crystal structure of the γ-TiAl phase, $[\bar{1}10]_\gamma$ and $\langle\bar{1}01]_\gamma$ directions are not equivalent. Thus, in the γ/α_2 lamellar structure, γ-TiAl can exist in six crystallographically-equivalent variants, each corresponding to one of the six possible orientations of the $[1\bar{1}0]_\gamma$ direction relative to the $\langle 11\bar{2}0\rangle_{\alpha 2}$ directions. As indicated schematically in Fig. 4, each γ-TiAl lamella is composed of a number of domains, with adjacent domains being different crystallographic variants of this phase. Since the probability for formation of each of these variants is expected to be the same, the properties of a γ-TiAl lamella in any close-packed direction in the $(111)_\gamma$ plane (the plane parallel to the lamellae interfaces) can be considered as identical. Using this approximation, one can distinguish between three types of slip systems in the lamellar γ-TiAl phase, Table I. Two of these (S1, S2) are denoted as soft-mode slip systems and are associated with slip parallel to the lamellae interfaces, while the third one (H1) is labeled as a hard-mode slip system and is associated with slip which has a component orthogonal to the

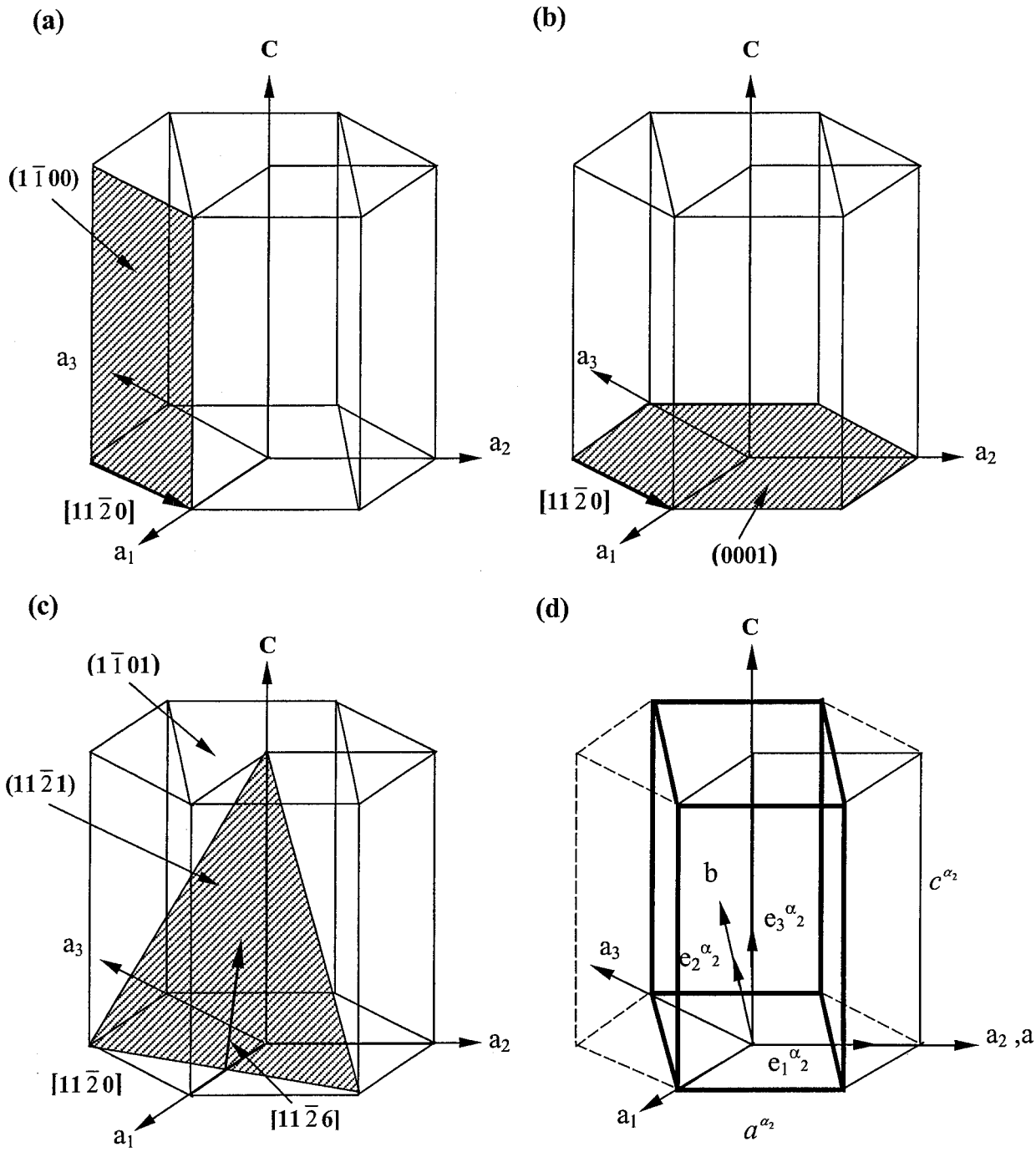

Figure 3 (a) Prismatic $\{10\bar{1}0\}\langle 1\bar{2}10\rangle$, (b) basal $(0001)\langle 11\bar{2}0\rangle$ and (c) pyramidal $\{11\bar{2}1\}\langle 11\bar{2}6\rangle$ slip systems in α_2-Ti_3Al: (d) The relationship between the simple hexagonal cell (light solid lines), the corresponding orthohexagonal cell (dark solid lines) and the hexagonal (prism) cell (dashed lines) in α_2-Ti_3Al.

lamellae interfaces. Propagation of slip in the direction normal to lamellae interfaces is deemed hard since, as discussed earlier, the α_2-Ti_3Al phase is kinematically constrained in that direction. An inspection of Table I establishes that in case of the S1 slip systems, the slip plane is parallel while in the case of the S2 slip systems, the slip plane is not parallel to the lamellar interface. In both cases, however, the slip direction resides in a plane parallel to the lamellar interface.

As far as plastic deformation of the α_2-Ti_3Al lamellae in polysynthetically-twinned γ-TiAl + α_2-Ti_3Al single crystals is concerned, it can be considered as essentially identical to that described in the previous section and is thus controlled by the three prismatic $\{10\bar{1}0\}\ \langle 1\bar{2}10\rangle$ and the three basal $(0001)\ \langle 11\bar{2}0\rangle$-$\langle a\rangle$- and by the six pyramidal $\{11\bar{2}1\}\langle 11\bar{2}6\rangle$–$\langle c+a\rangle$-slip systems.

2.3. Single-crystal crystal-plasticity materials constitutive model

The deformation behavior of γ-TiAl and α_2-Ti_3Al single crystals as well as of polysynthetically-twinned γ-TiAl + α_2-Ti_3Al single crystals are modeled using a rate-dependent, isothermal, elastic-viscoplastic, finite-strain, crystal-plasticity formulation. The continuum mechanics foundation for this model can be traced to the work of Teodosiu [12], Hill and Rice [13], Mandel [14], Teodosiu and Sidoroff [15], Asaro and Rice [16]

TABLE I Slip systems operating in γ-TiAl lamellae of polysynthetically-twinned γ-TiAl + α_2-Ti_3Al single crystals

Slip System	Symbol	Slip Type
$[1\bar{1}0](111)$ $[\bar{1}01](111)$ $[01\bar{1}](111)$	S1	Soft Mode
$[\bar{1}01](1\bar{1}1)$ $[1\bar{1}0](11\bar{1})$ $[0\bar{1}1](\bar{1}11)$	S2	Soft Mode
$[110](1\bar{1}1)$ $[011](1\bar{1}1)$ $[101](11\bar{1})$ $[011](11\bar{1})$ $[110](\bar{1}11)$ $[101](\bar{1}11)$	H1	Hard Mode

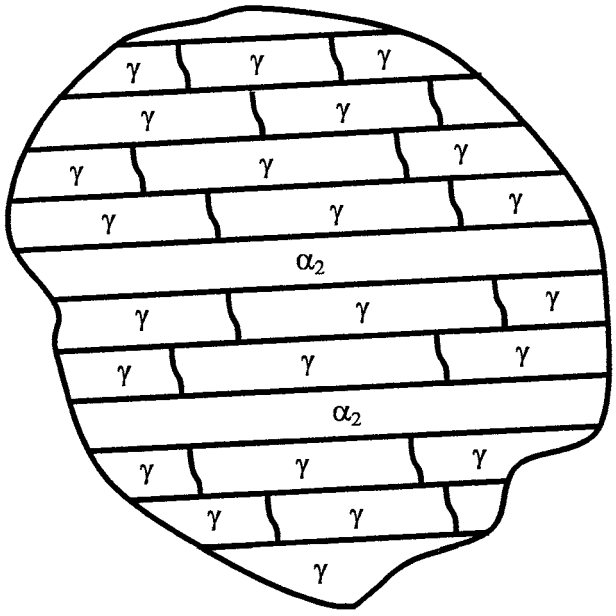

Figure 4 A schematic of the microstructure of polysynthetically-twinned γ-TiAl + α_2-Ti_3Al single crystals.

and Asaro [17]. The work of Kocks *et al*. [18], Frost and Ashby [19], and Argon [20], on the other hand, provides a more materials science viewpoint of the subject matter.

For each phase, the (initial) reference configuration consists of a perfect, stress-free crystal lattice and the embedded material, Fig. 5a. The position of each material point in the reference configuration is given by its position vector $\boldsymbol{X}$. In the current configuration, Fig. 5c, each material point is described by its position vector, $\mathbf{x}$, and hence, mapping of the reference configuration into the current configuration is described by the deformation gradient, $F = \mathrm{d}\mathbf{x}/\mathrm{d}\mathbf{X}$. As indicated in Fig. 5a–c, in order to reach the current configuration, the reference configuration must be deformed both elastically and plastically and, hence, the total deformation gradient can be multiplicatively decomposed into its elastic, F^{e}, and plastic, F^{P}, parts as $F = F^{\mathrm{e}}\,F^{\mathrm{p}}$. In other words, the deformation of a single-crystal material point is considered to be the result of two independent atomic-scale processes: (i) an elastic distortion of the crystal lattice corresponding to the stretching of atomic bonds

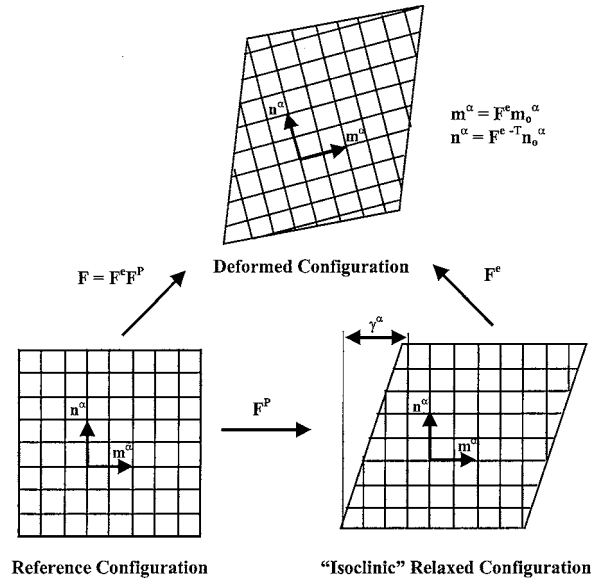

Figure 5 Multiplicative decomposition of the deformation gradient F into a plastic part F^{p} and an elastic part F^{e}. The unit slip plane normal n^α and the unit shear direction m^α are also indicated.

and; (ii) a plastic deformation which is associated with atomic plane slippage which leaves the crystal lattice undisturbed. While twinning is a potential inelastic deformation mechanism at lower temperatures and higher strain rates, only slip on well defined crystallographic planes in low-index crystallographic directions is considered in the present work.

The present constitutive model is based on the following governing variables: (i) The Cauchy stress, T; (ii) The deformation gradient, F; (iii) Crystal slip systems, labeled by integers α. Each slip system is specified by a unit slip-plane normal n_0^α, and a unit vector m_0^α aligned in the slip direction, both defined in the reference configuration; (iv) The plastic deformation gradient, F^{p}, with $\det F^{\mathrm{p}} = 1$ (plastic deformation by slip does not give rise to a volume change) and; (v) The slip system deformation resistance $s^\alpha > 0$ which has the units of stress.

Based on the aforementioned multiplicative decomposition of the deformation gradient, Fig. 5, the elastic deformation gradient F^{e} which describes the elastic distortions and rigid-body rotations of the crystal lattice, can be defined by:

$$F^{\mathrm{e}} \equiv FF^{\mathrm{p}-1}, \qquad \det F^{\mathrm{e}} > 0. \tag{1}$$

The plastic deformation gradient, F^{p}, on the other hand, accounts for the cumulative effect of shearing on all slip systems in the crystal.

Since elastic stretches in intermetallic materials are generally small, the constitutive equation for stress under isothermal conditions can be defined by the linear relation:

$$T^* = C[E^{\mathrm{e}}] \tag{2}$$

where C is a fourth-order anisotropic elasticity tensor, and E^{e} and T^* are respectively the Green elastic strain measure and the second Piola–Kirchoff stress measure relative to the isoclinic configuration obtained

after plastic shearing of the lattice as described by F^{p} in Fig. 5b. E^{e} and T^* are respectively defined as:

$$E^{\mathrm{e}} \equiv (1/2)\{F^{\mathrm{e}\mathrm{T}}F^{\mathrm{e}} - I\} \quad T^* \equiv (\det F^{\mathrm{e}})F^{\mathrm{e}-1}TF^{\mathrm{e}-T} \tag{3}$$

where I is the second order identity tensor.

The elasticity tensor C (expressed as a 6×6 square matrix), for the tetragonal γ-TiAl phase contains six independent non-zero components: $C_{11} = C_{22}$, C_{33}, C_{12}, $C_{13} = C_{23}$, $C_{44} = C_{55}$, and C_{66}. The hexagonal α_2-Ti_3Al phase exhibits transverse elastic isotropy and, hence, its elasticity tensor contains six different (five independent) non-zero components: $C_{11} = C_{22}$, C_{33}, C_{12}, $C_{23} = C_{13}$, $C_{44} = C_{55}$, $C_{66} = 0.5(C_{11} - C_{12})$. For both phases, the aforementioned elastic constants are defined relative to the respective orthonormal coordinate systems, Figs 2 and 3d.

The evolution equation for the plastic deformation gradient is defined by the flow rule:

$$\dot{F}^{\mathrm{p}}F^{\mathrm{p}-1} = \sum_{\beta} \dot{\gamma}^{\alpha} S_0^{\alpha}, \qquad S_0^{\alpha} \equiv m_0^{\alpha} \otimes n_0^{\alpha}, \tag{4}$$

where S_0^{α} is the Schmid tensor and $\otimes$ denotes the tensorial product of the two vectors.

The components of a unit slip plane normal n_0^{α} and a unit slip direction m_0^{α} in the respective reference configurations with respect to the orthonormal bases in the two phases are defined using the following procedure:

For a {h k l} ⟨u v w⟩ slip system in γ-TiAl:

$$\begin{aligned}
&\left\{n_{0,1}^{\alpha}, n_{0,2}^{\alpha}, n_{0,3}^{\alpha}\right\} = \{\mathrm{h}/\boldsymbol{a}^{\gamma}, \mathrm{k}/\boldsymbol{a}^{\gamma}, \mathrm{l}/\boldsymbol{c}^{\gamma}\}/\} \\
&\quad \times \{\mathrm{h}/\boldsymbol{a}^{\gamma}, \mathrm{k}/\boldsymbol{a}^{\gamma}, \mathrm{l}/\boldsymbol{c}^{\gamma}\}|; \\
&\left\langle m_{0,1}^{\alpha}, m_{0,2}^{\alpha}, m_{0,3}^{\alpha}\right\rangle = \langle \mathrm{u}\boldsymbol{a}^{\gamma}, \mathrm{v}\boldsymbol{a}^{\gamma}, \mathrm{w}\boldsymbol{c}^{\gamma}\rangle/| \\
&\quad \times \langle \mathrm{u}\boldsymbol{a}^{\gamma}, \mathrm{v}\boldsymbol{a}^{\gamma}, \mathrm{w}\boldsymbol{c}^{\gamma}\rangle|.
\end{aligned}$$

For a {h k m l} ⟨u v z w⟩ slip system in α_2-Ti_3Al:

$$\begin{aligned}
&\left\{n_{01}^{\alpha}, n_{02}^{\alpha}, n_{0.3}^{\alpha}\right\} = \{\mathrm{k}, -(\mathrm{k}+2\mathrm{h})/\sqrt{3}, l/(\boldsymbol{c}^{\alpha 2}/\boldsymbol{a}^{\alpha 2})\}/| \\
&\quad \times \{\mathrm{k}, -(\mathrm{k}+2\mathrm{h})/\sqrt{3}, 1/(\boldsymbol{c}^{\alpha 2}/\boldsymbol{a}^{\alpha 2})\}|; \\
&\left\langle m_{0,1}^{\alpha}, m_{0,2}^{\alpha}, m_{0,3}^{\alpha}\right\rangle = \langle 3\mathrm{v}/2, -\sqrt{3}(\mathrm{u}+\mathrm{v}/2), \\
&\quad \times \mathrm{w}(\boldsymbol{c}^{\alpha 2}/\boldsymbol{a}^{\alpha 2})\rangle|\langle 3\mathrm{v}/2, -\sqrt{3}(\mathrm{u}+\mathrm{v}/2), \\
&\quad \times \mathrm{w}(\boldsymbol{c}^{\alpha 2}/\boldsymbol{a}^{\alpha 2})\rangle|,
\end{aligned}$$

where | | is used to denote the magnitude of a vector or a plane normal.

The plastic shearing rate $\dot{\gamma}^{\alpha}$ on a slip system α is described using the following simple power-law relation:

$$\dot{\gamma}^{\alpha} = \dot{\tilde{\gamma}} \frac{|\tau^{\alpha}|^{1/m}}{|s^{\alpha}|} \mathrm{sign}\,(\tau^{\alpha}) \tag{5}$$

where $\dot{\tilde{\gamma}}$ is a reference plastic shearing rate, τ^{α} and s^{α} are the resolved shear stress and the deformation resistance on slip system α, respectively and m is the material rate-sensitivity parameter.

Since elastic stretches in intermetallic materials is generally small, the resolved shear stress on slip system α can be defined as:

$$\tau^{\alpha} = T^* \cdot S_0^{\alpha} \tag{6}$$

where the raised dot denotes the scalar product between two second order tensors.

Finally, the slip system resistance is taken to evolve as:

$$\dot{s}^{\alpha} = \sum_{\beta} \mathbf{h}^{\alpha\beta} |\dot{\gamma}^{\beta}|, \tag{7}$$

where $\mathbf{h}^{\alpha\beta}$ describes the rate of strain hardening on the slip system α due to the shearing on the coplanar (self-hardening) and non-coplanar (latent-hardening) slip systems β. A complete characterization of the hardening matrix $\mathbf{h}^{\alpha\beta}$ for the two phases is a formidable task. For example, in the α_2-Ti_3Al phase deforming by three equivalent prismatic {10 $\bar{1}$ 0} ⟨11 $\bar{1}$ 0⟩ ⟨a⟩-slip systems, three equivalent basal (0001) ⟨11$\bar{2}$0⟩ ⟨a⟩-slip systems and six equivalent pyramidal {10 $\bar{2}$ 1} ⟨11 $\bar{2}$ $\bar{6}$⟩ ⟨$c+a$⟩-slip systems, the $\mathbf{h}^{\alpha\beta}$ matrix contains $12 \times 12 = 144$ elements. In order to obtain a tractable description of the crystal hardening, the following simple form for the slip system hardening matrix $\mathbf{h}^{\alpha\beta}$ is adopted:

$$\mathbf{h}^{\alpha\beta} = \mathbf{q}^{\alpha\beta}\mathbf{h}^{\beta} \tag{8}$$

Here, $\mathbf{h}^{\beta}$ denotes the self-hardening rate while $\mathbf{q}^{\alpha\beta}$ is a matrix describing the latent hardening behavior. Since very little information is available in the literature regarding the latent hardening behavior of the two phases, a simple description for the matrix $\mathbf{q}^{\alpha\beta}$ is adopted:

$$\mathbf{q}^{\alpha\beta} = \begin{matrix} 1 \\ q_1 \end{matrix} \begin{cases} \text{if } \alpha \text{ and } \beta \text{ are coplanar slip systems,} \\ \text{otherwise} \end{cases} \tag{9}$$

Each phase has one set of coplanar slip systems and they are defined as following:

γ-TiAl Phase: One {111} ⟨1$\bar{1}$0], two {111} ⟨0$\bar{1}$1] and one {111} [11 $\bar{2}$] slip systems;

α_2-Ti_3Al Phase: Three basal ⟨a⟩-slip systems: (0001)[11 $\bar{2}$ 0], (0001)[$\bar{2}$ 110], (0001)[1 $\bar{2}$ 10].

In general, the parameter q_l can have different values depending on what types of slip systems interact. Due to lack of the relevant data, however, the approach of Kad *et al.* [8], is followed and a fixed value of $q_l = 1.4$ is used. Furthermore, following Kothari [21], the self-hardening rate $\mathbf{h}^{\beta}$ is defined as:

$$\mathbf{h}^{\beta} = h_0^{\beta} \left| 1 - \frac{s^{\beta}}{s_s^{\beta}} \right|^{\tau} \mathrm{sign}\left(1 - \frac{s^{\beta}}{s_s^{\beta}}\right). \tag{10}$$

where h_0^{β} is the initial hardening rate and s_s^{β} the saturation slip deformation resistance which may, in general, be different for different families of slip systems within the same phase. This variation, as well as the dependence of the saturation resistance s_s^{β} on strain rate and temperature, is not considered in the present work due to lack of the relevant data.

The integration of the material state represented by Equations 9, 10 and 12 along the loading path and its implementation in Abaqus/Explicit is discussed in Appendix A.

3. Results and discussion

3.1. Constitutive relations for γ-TiAl and α_2-Ti_3Al single crystals

In this section, the available experimental data for room-temperature deformation of γ-TiAl and α_2-Ti_3Al single crystals are used to determine their respective crystal-plasticity type materials constitutive relations.

The most comprehensive single study of the room-temperature deformation behavior of single-crystalline γ-TiAl known to the authors is the one carried out by Kawabata *et al.* [22]. Kawabata *et al.* [22] carried out uniaxial compression tests on five different orientations of γ-TiAl single crystals, Table II. Orientation of the compression axis is indicated in the first column of Table II. The slip systems with the maximum initial value of the Schmid factor are identified in the second column, while the respective magnitudes of the initial Schmid factors are given in the third column of the same table.

In accordance with the transmission electron microscopy observations of Kawabata *et al.* [22], only two types of slip systems are considered to be operational: the $\langle 1\bar{1}0]\ \{111\}$ and $\langle 10\bar{1}]\ \{111\}$ slip systems. The contribution of the $\langle \bar{1}\bar{1}2]\ \{111\}$ slip systems is deemed insignificant. The crystal-plasticity parameters (e.g. $\dot{\tilde{\gamma}}$ and m, Equation 10, h_0^β, s_s^β and r, Equation 15, etc.) are determined by fitting the room-temperature uniaxial-compression stress-strain curves obtained by Kawabata *et al.* [22] using the Simplex method. A brief overview of the Simplex method is given in Appendix B. All the crystal-plasticity parameters were determined by fitting the stress-strain curves corresponding to the [001] and [010] orientations of the uniaxial compression axis, Table II. A comparison between the two experimental and the two "fitted" uniaxial-compression stress-strain curves is shown in Fig. 6. Next, the same parameters are used to compute the stress-strain curves for the remaining three ($[\bar{1}10]$, $[\bar{2}96]$ and $[\bar{2}45]$) orientations of the uniaxial-compression axis. A comparison of these three stress-strain curves and their experimental counterparts is shown in Fig. 7.

TABLE II Crystallographic parameters for five γ-TiAl single-crystal orientations used in the work of Kawabata *et al.* [22]

Orientation of Compression Axis	Slip Systems with Maximum Initial Schmid Factor	Magnitude of Schmid Factor
[001]	Eight $\langle 10\bar{1}]\ \{111\}$	∼0.409
$[\bar{1}10]$	Four $\langle 10\bar{1}]\ \{111\}$	∼0.409
[010]	Four $\langle 1\bar{1}0]\ \{111\}$ Four $\langle 10\bar{1}]\ \{111\}$	∼0.409
$\sim[\bar{2}96]$	Single $[1\bar{1}0]\ (111)$	−0.482
$\sim[\bar{2}45]$	Single $[10\bar{1}]\ (111)$	−0.445

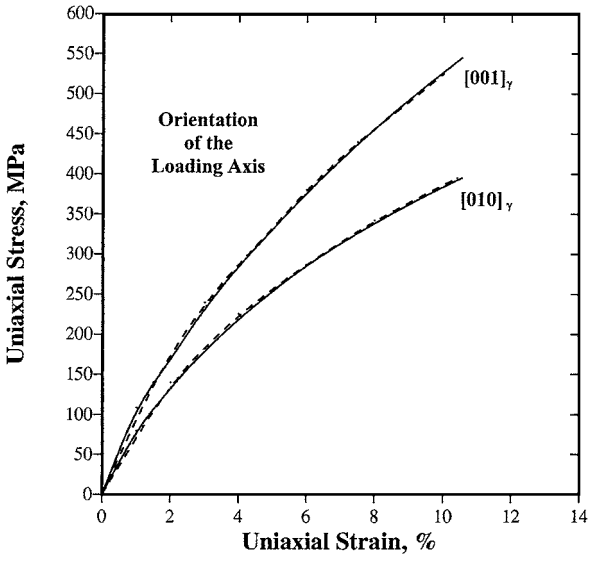

Figure 6 A comparison between the experimental uniaxial-compression stress-strain curves [22] (dashed lines) and the corresponding fitting curves (solid lines) based on the crystal-plasticity model used in the present work for two γ-TiAl single crystals.

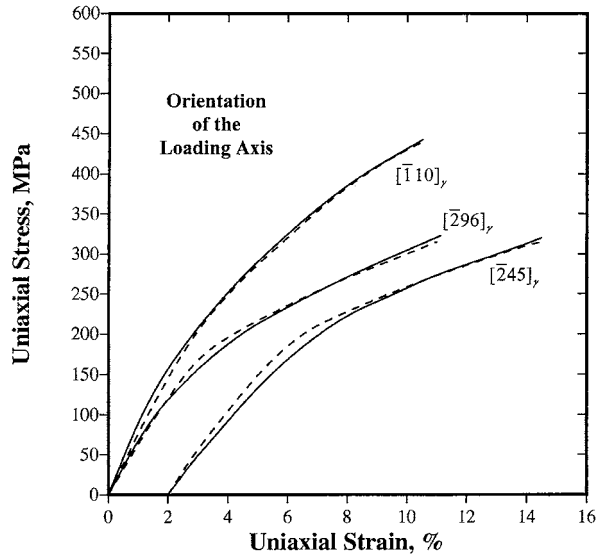

Figure 7 A comparison between the experimental uniaxial-compression stress–strain curves [22] (dashed lines) and the ones predicted by the current crystal-plasticity model (solid lines) for three γ-TiAl single crystals.

The agreement between the computed and experimental results shown in Figs 6 and 7 is quite good. It should be noted that for the last two orientations of the uniaxial-compression axis, Table II, plastic deformation is initially controlled by a single slip system. Hence, in these two cases, the effect of latent hardening (characterized by the magnitude of q_1), is insignificant. A good agreement between the experimental and the computed stress-strain curves in this case, Fig. 7, and an equally good agreement between the experimental and the computed stress-strain curves for the remaining three orientations of the uniaxial-compression axis, Figs 6 and 7, justifies the use of $q_1 = 1.4$.

The values of the crystal-plasticity-based materials constitutive parameters for single-crystalline γ-TiAl obtained in the present work as well as the remaining model parameters available in the literature are listed in Table III.

To determine the crystal-plasticity parameters for α_2-Ti_3Al single crystals, the simplex-based

TABLE III Crystal-plasticity parameters for the γ-TiAl single crystals

Parameter		Symbol	Value	Units	Reference
Elastic Constant		C_{11}	190	GPa	(23)
Elastic Constant		C_{33}	185	GPa	(23)
Elastic Constant		C_{12}	105	GPa	(23)
Elastic Constant		C_{13}	90	GPa	(23)
Elastic Constant		C_{44}	120	GPa	(23)
Elastic Constant		C_{66}	50	GPa	(23)
Reference Shearing Rate		$\dot{\gamma}_0$	0.005	s^{-1}	This Work
Strain Rate Sensitivity		m	0.014	N/A	This Work
Latent Hardening Parameter		q_l	1.4	N/A	This Work
Self-Hardening	$\{111\}\ 1/2\ \langle 1\bar{1}0]$	r	3.1	N/A	This Work
Exponent	$\{111\}\ \langle\bar{1}01]$		3.0		
Initial Slip	$\{111\}\ 1/2\ \langle 1\bar{1}0]$	s_0	14.3	MPa	This Work
Resistance	$\{111\}\ \langle\bar{1}01]$		22.7		
Self-Hardening	$\{111\}\ 1/2\ \langle 1\bar{1}0]$	h_o	940.2	MPa	This Work
Parameter	$\{111\}\ \langle\bar{1}01]$		950.7		
Saturation-Slip	$\{111\}\ 1/2\ \langle 1\bar{1}0]$	s_s	212.2	MPa	This Work
Resistance	$\{111\}\ \langle\bar{1}01]$		291.1		

TABLE IV Crystallographic parameters for five α_2-Ti_3Al single-crystal orientations used in the work of Inui *et al.* [24]. Euler Angles: $\omega = \phi = 0$ for All Orientations

Single-Crystal Orientation		Magnitude of Schmid Factor		
Orientation of Compression Axis	Euler Angle, θ	$(0001)\ \langle 11\bar{2}0\rangle$ Basal Slip	$\{1\bar{1}00\}\ \langle 11\bar{2}0\rangle$ Prismatic Slip	$\{11\bar{2}1\}\ \langle\bar{1}\bar{1}26\rangle$ Pyramidal Slip
[0001]	0	0	0	0.4494
$[11\bar{2}4]$	22	0.3449	0.0619	0.4459
$[11\bar{2}2]$	39	0.4889	0.1732	0.3321
$[11\bar{2}1]$	59	0.4454	0.3149	0.3995
$[11\bar{2}0]$	90	0	0.4330	0.4494

fitting procedure discussed above is applied to the room-temperature uniaxial-compression data of Inui *et al.* [24]. The crystallographic parameters for the five α_2-Ti_3Al single crystal orientations investigated by Inui *et al.* [24] are listed in Table V. Each orientation is defined in terms of its Euler angles (ω, θ, and ϕ), where the angles are listed in the order of the rotations they quantify. For all five α_2-Ti_3Al single-crystal orientations studied by Inui *et al.* [24], $\omega = \phi = 0^\circ$, while $0 \leq \theta \leq 90^\circ$. As indicated in Table IV, when the basal plane is normal to the compression axis, ($\theta = 0^\circ$), the Schmid factor for the basal $(0001)\langle 11\bar{2}0\rangle$ and the prismatic $\{1\bar{1}00\}\ \langle 11\bar{2}0\rangle$ $\langle a\rangle$-slip systems is zero and, hence, only the pyramidal $\{11\bar{2}1\}\ \langle\bar{1}\bar{1}26\rangle$ $\langle c+a\rangle$–slip systems are operative. Hence the uniaxial-compression stress-strain curve for the $\theta = 0^\circ$ orientation of the α_2-Ti_3Al single crystal is used to determine the crystal-plasticity parameters for the pyramidal $\{11\bar{2}1\}\ \langle\bar{1}\bar{1}26\rangle$ $\langle c+a\rangle$-slip. In the case of the $\theta = 90^\circ$ orientation of the compression axis, the Schmid factor for the $(0001)\ \langle 11\bar{2}0\rangle$ basal slip is still zero. Hence the stress-strain curve for this orientation crystal is used to determine the crystal-plasticity parameters for the $\{1\bar{1}00\}\ \langle 11\bar{2}0\rangle$ prismatic slip system. Lastly, the stress-strain curve corresponding to the $\theta = 39^\circ$ orientation of the α_2-Ti_3Al single crystal is used to determine the crystal-plasticity parameters for the $(0001)\ \langle 11\bar{2}0\rangle$ slip systems. The results of the aforementioned fitting procedure are summarized in Fig. 8. The crystal-plasticity parameters for the α_2-Ti_3Al single crystal obtained as well as the remaining

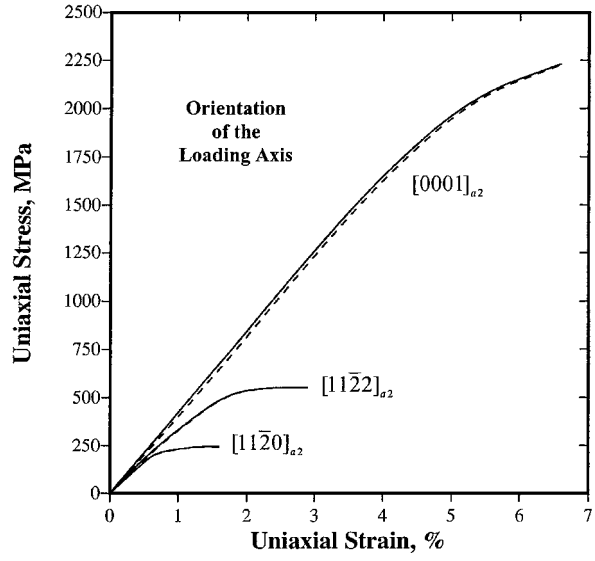

Figure 8 A comparison between the experimental uniaxial-compression stress–strain curves [24] (dashed lines) and the corresponding fitting curves (solid lines) based on the current crystal-plasticity model (solid lines) for three α_2-Ti_3Al single crystals.

parameters available in the literature are summarized in Table V.

The crystal-plasticity parameters obtained are used to predict the uniaxial-compression stress-strain curves for the remaining two orientations of α_2-Ti_3Al single crystal ($\theta = 22^\circ$ and $\theta = 59^\circ$) investigated by Inui *et al.* [24]. A comparison of the predicted and the

TABLE V Crystal-plasticity parameters for the α_2-Ti_3Al single crystals

Parameter		Symbol	Value	Units	Reference
Elastic Constant		C_{11}	221	GPa	(25)
Elastic Constant		C_{33}	238	GPa	(25)
Elastic Constant		C_{12}	71	GPa	(25)
Elastic Constant		C_{13}	85	GPa	(25)
Elastic Constant		C_{44}	69	GPa	(25)
Reference Shearing Rate		$\dot{\gamma}_0$	0.001	s^{-1}	This Work
Strain Rate Sensitivity		m	0.009	N/A	This Work
Latent Hardening Parameter		q_l	1.4	N/A	This Work
Self-Hardening	$\{1\bar{1}00\}\langle 11\bar{2}0\rangle$	r	2.7	N/A	This Work
Exponent	$(0001)\langle 11\bar{2}0\rangle$		3.0		
	$\{11\bar{2}1\}\langle 11\bar{2}6\rangle$		2.9		
Initial Slip	$\{1\bar{1}00\}\langle 11\bar{2}0\rangle$	s_0	19.2	MPa	This Work
Resistance	$(0001)\langle 11\bar{2}0\rangle$		44.8		
	$\{11\bar{2}1\}\langle 11\bar{2}6\rangle$		121.9		
Self-Hardening	$\{1\bar{1}00\}\langle 11\bar{2}0\rangle$	h_o	861.7	MPa	This Work
Parameter	$(0001)\langle 11\bar{2}0\rangle$		742.8		
	$\{11\bar{2}1\}\langle 11\bar{2}6\rangle$		814,7		
Saturation Slip	$\{1\bar{1}00\}\langle 11\bar{2}0\rangle$	s_s	149.3	MPa	This Work
Resistance	$(0001)\langle 11\bar{2}0\rangle$		417.7		
	$\{11\bar{2}1\}\langle 11\bar{2}6\rangle$		1586.3		

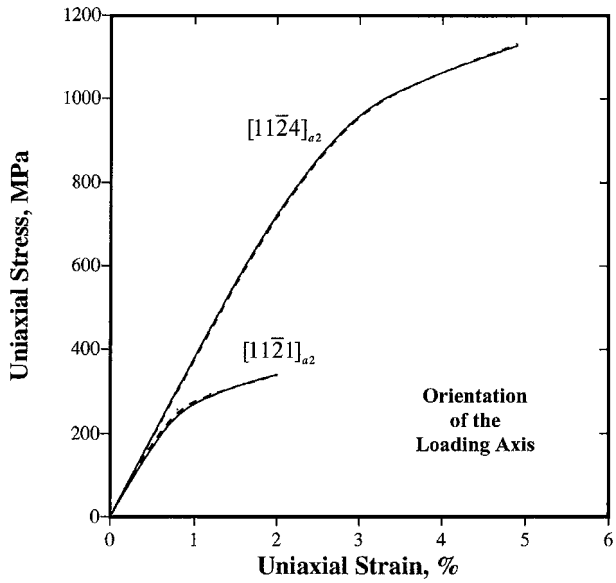

Figure 9 A comparison between the experimental uniaxial-compression stress–strain curves [24] (dashed lines) and the corresponding curves predicted by the current crystal-plasticity model (solid lines), for two α_2-Ti_3Al single crystals.

experimental stress-strain curves shown in Fig. 9 suggests that the crystal-plasticity parameters determined in the present work quite realistically account for the deformation behavior of α_2-Ti_3Al single crystals at room temperature.

3.2. Polysynthetically-twinned γ-TiAl + α_2-Ti_3Al single crystals

Macroscopic deformation behavior of a multiphase material with complex microstructure such as polysynthetically-twinned γ-TiAl + α_2-Ti_3Al single crystals can be modeled using the finite element method. This entails (a) a finite-element discretization of the materials microstructure; (b) the knowledge of materials constitutive relations of the constituent phases; (c) information pertaining to the orientation relationship between the phases; and (d) a quantitative understanding of kinematic constraints, e.g., the crystallographic nature of the habit plane separating adjacent particles of the phases. The typical microstructure of γ-TiAl + α_2-Ti_3Al single crystals, Fig. 4, can be readily discretized into finite elements. The γ-TiAl/α_2-Ti_3Al orientation relationship, materials constitutive relations for the two phases and the habit plane conditions are all discussed in the previous sections. Thus, a finite element analysis of the deformation behavior of polysynthetically-twinned γ-TiAl + α_2-Ti_3Al single crystals can be carried out. However, this was not done here because the ultimate objective of the present work is to develop materials constitutive relations for polysynthetically-twinned γ-TiAl + α_2-Ti_3Al single crystals suitable for implementation into a finite element analysis of macroscopic deformation behavior of polycrystalline forms of these materials. In such analyses, one cannot typically afford to discretize a multigrain (multi colony) material into finite elements and assign to each element the properties of a single phase (γ-TiAl or α_2-Ti_3Al). Rather, one needs homogenized, effective properties of polysynthetically-twinned γ-TiAl + α_2-Ti_3Al single crystals. In this section, an attempt is made to derive such effective constitutive relations of polysynthetically-twinned γ-TiAl + α_2-Ti_3Al single crystals and test these relations against their experimental counterparts.

As discussed in Section 2.2, plastic deformation in polysynthetically-twinned γ-TiAl + α_2-Ti_3Al single crystals parallel to the interlamellar γ-TiAl/α_2-Ti_3Al interfaces is substantially easier (the soft mode) than deformation which has a component normal to these interfaces (the hard mode). Therefore, the two modes of deformation will be considered separately.

In γ-TiAl lamellae, plastic deformation on planes parallel to the $(111)_\gamma \parallel (0001)_{\alpha 2}$ boundaries is controlled both by the $\langle 1\bar{1}0]$ (111) and the $\langle 10\bar{1}]$ (111)

(S1)-slip systems, Table I. As shown in Section 3.1, slip resistance and strain hardening characteristics differ in these two slip systems. Also as shown in Fig. 4, each γ-TiAl lamella consists of multiple crystallographically-equivalent domains. The γ-TiAl domains differ from each other relative to along which of the six $\langle 11\bar{2}0\rangle$ directions of the α_2-Ti_3Al phase is $\langle 10\bar{1}]$ direction of the γ-TiAl aligned in the $(111)_\gamma \parallel (0001)_{\alpha 2}$ interlamellar boundary. Since the probability for the formation of each domain is the same, the effective slip properties of γ-TiAl lamella are expected to be essentially the same in all close-packed directions in the (111) plane parallel to the interlamellar boundaries. Since there are twice as many $\langle 10\bar{1}]$ directions as $\langle 1\bar{1}0]$ directions in a (111) plane, and the probability for occurrence of each domain in a γ-TiAl lamella is expected to be the same, the effective properties for the S1 soft-mode deformation of the γ-TiAl lamellae are set equal to a weighted average of those associated with $\langle 1\bar{1}0]$ (111) (weighting factor $=$ 1/3) and $\langle 10\bar{1}]$ (111) (weighting factor $=2/3$) slip systems.

The S2 soft-mode plastic deformation of γ-TiAl lamellae, Table I, involves slip in the close-packed directions parallel to the interlamellar boundaries but on planes inclined with respect to these boundaries. Consequently, the deformation resistance for S2 slip is expected to be higher than that for S1 slip and the former is determined using the available deformation data for polysynthetically-twinned γ-TiAl $+ \alpha_2$-Ti_3Al single crystals.

As indicated in Table I, S2 slip involves both $\langle 1\bar{1}0]$ and $\langle 10\bar{1}]$ slip directions which are associated with different deformation resistances and hardening characteristics. Hence, the weighted-average approach discussed above is also applied to S2 slip. To account for the effect of inclination of the slip planes involved in S2 slip with respect to the lamellar interface, the initial slip resistance for S2 slip is set to be α times that of S1 slip where $\alpha > 1$. The contribution of plastic deformation in α_2-Ti_3Al parallel to the $(111)_\gamma \parallel (0001)_{\alpha 2}$ lamellar boundaries is not considered for the following reasons: (a) The soft-mode plastic deformation is expected to be dominated by the softer (γ-TiAl) phase; and (b) since the volume fraction of the α_2-Ti_3Al lamellae is typically an order of magnitude smaller than that of the γ-TiAl lamellae, the role of α_2-Ti_3Al in the soft-mode deformation is expected to be minimal.

The situation is quite different for the hard mode of plastic deformation, i.e., for plastic deformation, which includes a component normal to the $(111)_\gamma \parallel (0001)_{\alpha 2}$ lamellar boundaries. In this case slip is controlled by the phase which exerts more resistance toward this mode of plastic deformation, the α_2-Ti_3Al phase. As discussed in Section 3.1, the only slip system in α_2-Ti_3Al which gives rise to this type of plastic deformation is the $\{11\bar{2}1\}$ $\langle 11\bar{2}6\rangle$-$\langle c+a\rangle$ slip system. Hence, this slip system is expected to control the hard-mode of plastic deformation in polysynthetically-twinned γ-TiAl $+ \alpha_2$-Ti_3Al single crystals. However, since the volume fraction of α_2-Ti_3Al is typically only one tenth of that of γ-TiAl, and γ-TiAl appears as multiple lamellae, limited hard-mode plastic deformation in γ-TiAl is possible. This possibility is incorporated implicitly by allowing the $\{11\bar{2}1\}$ $\langle 11\bar{2}6\rangle$ slip systems in α_2-Ti_3Al to have a lower deformation resistance relative to the ones derived in Section 3.2. The ratio of the two resistances is defined as β, where $\beta < 1$. Nevertheless, the $\{11\bar{2}1\}$ $\langle 11\bar{2}6\rangle$ slip system is considered as the only slip system providing for plastic deformation in the direction normal to the lamellar interfaces.

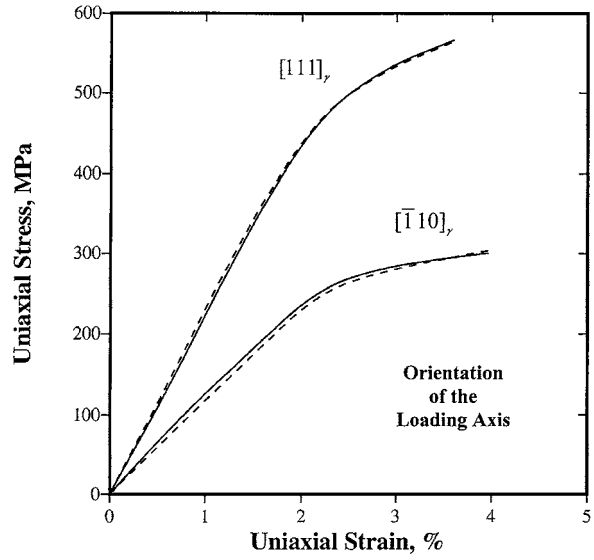

Figure 10 A comparison between the experimental uniaxial-compression stress–strain curves [26] (dashed lines) and the corresponding fitting curves (solid lines) based on the current crystal-plasticity model for two γ-TiAl $+ \alpha_2$-Ti_3Al single crystals.

To summarize, the plastic deformation behavior of γ-TiAl and α_2-Ti_3Al lamellae in polysynthetically-twinned γ-TiAl $+ \alpha_2$-Ti_3Al materials is for the most part taken to be identical to that of their single-crystalline counterparts presented in Section 3.1. In fact, experimental data for room-temperature deformation behavior of polysynthetically-twinned γ-TiAl $+ \alpha_2$-Ti_3Al single crystals are used to determine only two parameters: α which the initial deformation resistance for the S2 and β which quantifies the initial deformation resistance for $\{11\bar{2}1\}$ $\langle 11\bar{2}6\rangle$ slip. These parameters are determined by fitting the uniaxial-compression stress-strain curves of Fujiwara *et al.* [26] using the aforementioned Simplex method. They are found to be $\alpha = 1.23$ and $\beta = 0.86$. A comparison of two fitting stress-strain curves and their experimental counterparts are shown in Fig. 10. The orientation of the compression axis relative to the γ-TiAl phase is indicated in Fig. 10. The crystal plasticity parameters obtained are next used to predict room-temperature stress-strain curves for three additional orientations of polysynthetically-twinned γ-TiAl $+ \alpha_2$-Ti_3Al single crystals investigated by Fujiwara *et al.* [26]. A comparison of three predicted uniaxial-compression stress-strain curves and their experimental counterparts, along with the orientations of the compression axis relative to the γ-TiAl phase are shown in Fig. 11. A very good agreement between the two sets of curves in Fig. 11 suggests that the crystal plasticity model adopted and

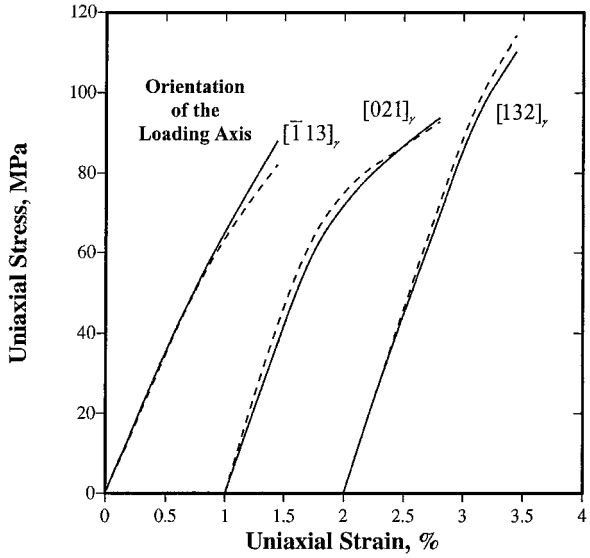

Figure 11 A comparison between the experimental uniaxial-compression stress–strain curves [26] (dashed lines) and the corresponding predicted curves (solid lines) based on the current crystal-plasticity model for three γ-TiAl + α_2-Ti_3Al single crystals.

the associated parameters assessed in the present work can capture the main features of deformation behavior of polysynthetically-twinned γ-TiAl + α_2-Ti_3Al single crystals, at least under the uniaxial loading conditions.

4. Conclusions

In the present work a three-dimensional, isothermal, rate-dependent, viscoplastic, finite-strain, crystal-plasticity model is adopted to simulate deformation behavior of polysynthetically-twinned γ-TiAl + α_2-Ti_3Al single crystals at room-temperature. The model parameters are determined by fitting the available uniaxial-compression stress-strain curves for both γ-TiAl and α_2-Ti_3Al single crystals and γ-TiAl + α_2-Ti_3Al polysynthetically-twinned single crystals using a basic Simplex optimization algorithm. Based on the results obtained the following conclusions can be made:

1. The crystal-plasticity model adopted can quite well account for the observed deformation behavior of both γ-TiAl and α_2-Ti_3Al single crystals and γ-TiAl + α_2-Ti_3Al polysynthetically-twinned single crystals at least under the uniaxial loading conditions considered.
2. The deformation resistance for the $\{11\bar{2}1\}\langle 11\bar{2}6\rangle$ slip systems is exceptionally high (Table V), validating that the α_2-Ti_3Al phase is essentially kinematically constrained in the c-direction.
3. As expected, the deformation resistance for the $\langle 1\bar{1}0]$ ordinary-dislocation slip is lower than that for the $\langle\bar{1}01]$ super-dislocation slip, Table III.
4. The homogenization procedure proposed, in which the soft-mode deformation behavior is assumed to be controlled by the softer (γ-TiAl) phase while the hard–mode behavior by the hard (α_2-Ti_3Al) phase, yields a reasonably good effective deformation behavior of polysynthetically-twinned γ-TiAl + α_2-Ti_3Al single crystals.

Acknowledgements

The material presented here is based on work supported by the National Science Foundation, Grant Numbers DMR-9906268 and CMS-9531930 and by the U.S. Army Grant Number DAAH04-96-1-0197. The authors are indebted to Drs. Bruce A. MacDonald and Daniel C. Davis of NSF and Dr. David M. Stepp of ARO for the continuing interest in the present work. The authors also acknowledge the support of the Office of High Performance Computing Facilities at Clemson University.

Appendix A: Integration of the Material State

The single-crystalline material constitutive model discussed in Section 2.3 is implemented in a Vectorized User Material Subroutine (VUMAT) of the commercial finite element program ABAQUS/Explicit [11]. At the beginning of each time increment, (time $= t$), for each element and each integration point, Abaqus/Explicit calls the VUMAT subroutine and provides it with the following information:

(i) A list of materials parameters such as the ones listed in Tables III or V;
(ii) The time-independent slip system parameters (m_0^α, n_0^α), as discussed in Sections, 2.1 and 2.2;
(iii) A list of variables: $\{F(t),\ F^{\mathrm{p}}(t),\ s^\alpha(t),\ T(t)\}$; and
(iv) A kinematic estimate of the deformation gradient $F(\tau)$ at the end of the time increment (time $= \tau = t + \Delta t$).

Within the VUMAT, a stable, accurate and efficient computational procedure based on an Euler forward integration scheme is used to determine the variables $F^{\mathrm{p}}(\tau)$, $s^\alpha(\tau)$, and $T(\tau)$ at the end of the time increment. The procedure involves the following major steps:

(1) An inverse of the plastic deformation gradient, $F^{\mathrm{p}^{-1}}(\tau)$, is first computed as:

$$F^{\mathrm{e}}(t) = F(t)F^{\mathrm{p}^{-1}}(t) \tag{A.1}$$

$$E^{\mathrm{e}}(t) = \frac{1}{2}\{F^{\mathrm{e}}(t)^T F^{\mathrm{e}}(t) - I\};\ T^*(t) = C(E^*(t)) \tag{A.2}$$

$$\tau^\alpha(t) = T^*(t)\cdot S_0^\alpha \tag{A.3}$$

$$\Delta\gamma^\alpha(t) = \dot{\bar{\gamma}}\left|\frac{\tau^\alpha(t)}{S^\alpha(t)}\right|^{\frac{1}{m}}\Delta t \tag{A.4}$$

$$F^{\mathrm{p}^{-1}}(\tau) \cong F^{\mathrm{p}^{-1}}(t)\left\{I - \sum_\alpha \Delta\gamma^\alpha(t)S_0^\alpha\right\} \tag{A.5}$$

(2) Next, the Cauchy stress $T(\tau)$ at the end of the time increment is computed as:

$$F^{\mathrm{e}}(\tau) = F(\tau)F^{\mathrm{p}^{-1}}(\tau) \tag{A.6}$$

$$E^{\mathrm{e}}(\tau) = \frac{1}{2}\{F^{\mathrm{e}}(\tau)^T F^{\mathrm{e}}(\tau) - I\};\ T^*(\tau) = C(E^*(\tau)) \tag{A.7}$$

$$T(\tau) = \det\left(F^*(\tau)\right)^{-1} F^*(\tau) T^*(\tau) F^*(\tau)^T \quad \text{(A.8)}$$

(3) Finally, the slip resistances $s^\alpha(\tau)$ are updated as:

$$\mathbf{h}^{\alpha\beta}(t) = \mathbf{q}^{\alpha\beta} \left| 1 - \frac{s^\beta(t)}{s_s} \right|^r \operatorname{sign}\left\{ 1 - \frac{s^\beta(t)}{s_s} \right\} \quad \text{(A.9)}$$

$$s^\alpha(\tau) = s^\alpha(t) + \sum_\beta \mathbf{h}^{\alpha\beta}(t) |\Delta\gamma^\beta(t)| \quad \text{(A.10)}$$

and a list of variables: $\{F^{\mathrm{p}}(\tau),\ s^\alpha(\tau),\ T(\tau)\}$ is passed back to Abaqus/Explicit.

Appendix B: Basic simplex method

Crystal-plasticity materials constitutive parameters listed in Tables III and V are determined using the basic Simplex search method [27]. The basic Simplex search method requires that the number of initial evaluations of the objective function (designs in the following) be one greater than the number of design variables. The following objective function, which should be minimized, is defined in the present work as:

$$G = \sum_{i=1}^{M} \left(\sigma_1 - \sigma_i^{\mathrm{exp.}} \right) \quad \text{(B1)}$$

where M is the number of discrete stress-strain values used to represent the corresponding stress-strain curve and σ_i and $\sigma_i^{\mathrm{exp.}}$ respectively represent the computed and the experimental uniaxial-compressive stress at a given value of the uniaxial-compressive strain. In the case of [001]-oriented γ-TiAl single crystals, Table II, there are 6 design variables ($\dot{\tilde{\gamma}}_0$, m, r, s_0, h_0, and s_s) and hence the Simplex method entails that the objective function be initially evaluated for 7 sets of design variables. In the 6-dimensional search space, the 7 initial design variables form a 7-vertex geometric figure, which is generally referred to as the *initial simplex*. The initial designs are ranked according to the magnitude of the objective function. The design with the maximum value of the objective function is ranked as worst. Next, the worst design is reflected through the centroid of the remaining designs to obtain a new design. The new design replaces the prior worst design and a new simplex is formed. The designs within the new simplex are ranked again and the procedure is continued. To prevent the method from bouncing back and forth between two designs in cases when the new design is the worst design within the new simplex, the algorithm selects the second worst design and reflects it in such cases. The main advantage of the simplex method is that it requires the evaluations of the objective function but not of its derivatives. Furthermore, after the initial simplex is formed, one evaluation of the objective function per search step is needed. In addition, the algorithm is very simple and easily coupled with a commercial finite element program such as Abaqus/Explicit. The main limitation of the simplex method is that, like many other search algorithms, it may stall at a local minimum. To overcome this limitation, the Simplex method must be started with different initial simplexes and the resulting minima ranked. Another potential limitation of the method is that it may require rescaling of the design variables to make them all of the same order of magnitude, since all variables are subjected to the same reflection distance. Furthermore, the search progress can be slow if the number of design variables is large. To overcome these limitations of the basic Simplex method, Nelder and Mead [28] introduced several modifications, which enable expansion or contraction of the simplex in a direction in which the optimization conditions are favorable. This modification is practical when the number of design variables is large and when evaluation of the objective function is not time consuming. Since in the present work, the number of design variables is relatively small and the evaluation of the objective function involves a finite element simulation by Abaqus/Explicit and post processing of the results, which are more time consuming, the basic Simplex search method is used.

References

1. M. YAMAGUCHI and Y. UMAKOSHI, *Prog. Mater. Sci.* **34** (1990) 1.
2. L. A. JOHNSON, D. P. POPE and J. O. STIEGLER (eds.), in Materials Research Society Symposium Proceedings, Vol. 213, Pittsburgh, Pennsylvania, 1991.
3. S. H. WHANG, C. T. LIU, D. P. POPE and J. O. STIEGLER (eds.), "High-temperature Aluminides and Intermetallics" (The Minerals, Metals and Materials Society, Warrendale, Pennsylvania, 1990).
4. Y. S. YANG and S. K. WU, *Phil. Mag.* **65** (1992) 15.
5. H. INUI, M. H. OH, A. NAKAMURA and M. YAMAGUCHI, *Acta Metall.* **40** (1992) 3095.
6. T. FUJIWARA, A. M. NAKAMURA, M. HOSOMI, S. R. NISHITANI, Y. SHIRAI and M. YAMAGUCHI, *Phil. Mag. A* **61** (1990) 591.
7. T. NAKANO, A. YOKOYAMA and Y. UMAKOSHI, *Scripta Metall.* **27** (1992) 1253.
8. B. K. KAD, M. DAO and R. J. ASARO, *Phil. Mag. A* **71** (1995) 567.
9. M. DAO, B. K. KAD and R. J. ASARO, *ibid A* **74** (1996) 569.
10. B. J. LEE, B. K. KAD and R. J. ASARO, *Scripta Metall.* **29** (1993) 823.
11. Abaqus/Explicit 5.8 User Manual (Hibbit, Karlsson & Sorenson, Inc., Providence, RI, 1998).
12. C. TEODOSIU, in Proceedings of the Conference on Fundamental Aspects of Dislocation Theory, edited by R. Simmons, J. A. DeWit and R. Bullough (McMillan, London, 1970) p. 837.
13. R. HILL and J. R. RICE, *Journal of the Mechanics and Physics of Solids* **20** (1972) 401.
14. J. MANDEL, in Proceedings of the International Symposium on Foundations of Continuum Thermodynamics, edited by D. Domingos, J. J. Nina and J. H. Whitlaw (McMillan, London, 1974) p. 283.
15. C. TEODOSIU and F. SIDOROFF, *International Journal of Engineering Science* **14** (1976) 165.
16. R. J. ASARO and J. R. RICE, *Journal of the Mechanics and Physics of Solids* **25** (1977) 309.
17. R. J. ASARO, *ASME Journal of Applied Mechanics* **50** (1983) 921.
18. U. F. KOCKS, A. S. ARGON and M. F. ASHBY, *Progress in Material Science* **19** (1975) 1.
19. H. J. FROST and M. F. ASHBY, "Deformation Mechanism Maps" (Pergamon Press, New York, 1982).
20. A. S. ARGON, in "Physical Metallurgy," edited by R. W. Cahn and P. Haasen (Elsevier, Amsterdam, 1995).
21. M. KOTHARI, Ph.D Thesis, MIT, June 1997.
22. T. KAWABATA, T. KANAI and O. IZUMI, *Acta Metall.* **33** (1985) 1355.
23. C. L. FU and M. H. YOO, *Phil. Mag. Lett.* **62** (1990) 159.
24. H. INUI, Y. TODA and M. YAMAGUCHI, *Phil. Mag. A* **67** (1993) 1315.

25. M. H. YOO, J. ZOU and C. L. FU, *Mater. Sci. Eng.* **A192** (1995) 14.
26. T. FUJIWARA, A. NAKAMURA, M. HOSOMI, S. R. NISHITANI, Y. SHIKAI and M. YAMAGUCHI, *Philosophical Magazine A* **61** (1990) 591.
27. WALTERS, PARKER, MORGAN and DEMING, in "Sequential Simplex Optimization: A Technique for Improving Quality and Productivity of Research, Development and Manufacturing" (CRC Press, New York, 1991).
28. J. A. NELDER and R. A. MEAD, *Computer Journal* **7** (1965) 308.

Received 24 October 2000
and accepted 10 January 2001